

Fast resolving Galactic binaries in LISA data and its ability to study the Milky Way

Pin Gao,¹ Xi-Long Fan,^{2,*} Zhou-Jian Cao,¹ and Xue-Hao Zhang³

¹*Department of Astronomy, Beijing Normal University, Beijing 100875, China*

²*School of Physics and Technology, Wuhan University, Wuhan 430072, China*

³*Institute of Theoretical Physics and Research Center of Gravitation, Lanzhou University, Lanzhou 730000, China*

Resolving individual gravitational waves from tens of millions of double white dwarf (DWD) binaries in the Milky Way is a challenge for future space-based gravitational wave detection programs. By using previous data to define the priors for the next search, we propose an accelerated approach of searching the DWD binaries, and demonstrate its efficiency based on the GBSIEVER detection pipeline. Compared to the traditional GBSIEVER method, our method can obtain $\sim 50\%$ of sources with 2.5% of the searching time for LDC1-4 data. In addition, we find that both methods have a similar ability to detect the Milky Way structure by their confirmed sources. The relative error of distance and chirp mass is about 20% for DWD binaries whose gravitational wave frequency is higher than 4×10^{-3} Hz, even if they are close to the Galactic centre. Finally, we propose a signal-to-noise ratio (SNR) threshold for LISA to confirm the detection of DWD binaries. The threshold should be 16 when the gravitational wave frequency is lower than 4×10^{-3} Hz and 9 when the frequency range is from 4×10^{-3} Hz to 1.5×10^{-2} Hz.

I. INTRODUCTION

The first direct detection of gravitational wave (GW) from a binary black hole merger by the Laser Interferometer Gravitational-Wave Observatory (LIGO) gives us access to a new messenger and opens the era of observational gravitational wave astronomy [1]. For lower frequencies, we have to increase the arm length of the gravitational wave detector and avoid the influence of ground noise. Laser Interferometric Space Antenna (LISA) [2–4], Taiji [5–7] and Tianqin [8–10] are proposed in this context. They are space-based gravitational wave detectors and have a sensitive frequency domain from 10^{-4} Hz to 10^{-1} Hz, where there are rich sources of GW, such as coalescing massive black holes, ultracompact galactic binaries, and extreme mass ratio inspirals [2, 11].

For space-based gravitational wave detectors, data processing is a challenge. There are numerous ($\sim 10^7$) Galactic binary gravitational wave sources [12] whose signals span the whole LISA band. Most of them are double white dwarf (DWD) binaries. Though DWD signals are simple: nearly constant amplitude sine function with a small amount of change in frequency, the enormous quantity of them, as well as the instrument's frequency and amplitude modulations, make it difficult to break them down. In the last two decades, a series of LISA data challenges have been organized to prepare the LISA data analysis techniques. The first four challenges are called mock LISA data challenges (MLDCs) [13–16], followed by a series called LISA data challenge (LDC) [17]. The LDC1 contains several sections, among which LDC1-4 is our concern's galactic binary gravitational waves. The data contains about 30 million binary systems and mock LISA instrumental noise with a signal sampling period of 15 seconds. The total duration of the data is two years

(62914560 seconds). Several data analysis methods have been proposed [18–28]. Some of them are relatively mature:

- (1) The blocked-annealed Metropolis–Hasting (BAM) algorithm combined with simulated annealing and Markov chain Monte Carlo (MCMC) has been optimized to search for tens of thousands of overlapping signals across the LISA band and performed almost flawlessly on all the round 1 Mock LISA Data Challenge data sets. In a blockwise frequency search, they report about 20000 sources in MLDC-2.1 data which had 26 million DWD binaries [20].
- (2) An extension of BAM incorporating transdimensional MCMC was tested on the training data from MLDC-4 and reported approximately 9000 sources in the [0, 10] mHz band with a detection rate of about 90% [23].
- (3) An iterative source subtraction with a maximum likelihood detection method reported about 12000 sources in MLDC-3.1 data, which contains 60 million DWD binaries [24].
- (4) An interesting new approach that aims to create a time-evolving source catalogue rather than using them all at once has been opened recently. In real detection, as LISA data accumulates, this approach could be of great use [25].
- (5) Particle swarm optimization (PSO) is used in Galactic binary separation by iterative extraction and validation using extended range (GBSIEVER) [22]. In the [0.1, 15] mHz frequency domain, the method can find sources from 9291 to 12270, corresponding to the detection rate of 90.26% and 84.16%, respectively.
- (6) Bayesian approaches are computationally expensive to extract tens of thousands of signals. The

* xilong.fan@whu.edu.cn

authors first find the maximum likelihood estimate and then compute the posterior distribution around the identified maximum likelihood estimate to give a more informative solution [26].

- (7) An iterative combinatorial algorithm to search for double white dwarfs in MLDC-3.1 data quickly determine the rough parameters of the target sources in a coarse search process. After that, a fine search process (Particle Swarm Optimization) is used to further determine the parameters of the signals based on the coarse search [27].

Until now, most search methods directly search the whole 2-year mock data and found about 10^4 candidates. However, waiting for LISA to return all the data before searching is impractical. In fact, once the LISA mission begins taking data, the data analysis could continuously add small chunks of new data to the existing data set, then use previous results to define the priors for the next search. Here we propose an accelerated approach depending on the early search results from the previous LISA data. Similar idea has been used for existing time-evolving LISA Galactic binary GWs extraction algorithm [25]. We demonstrate our approach based on the GB-SIEVER detection pipeline [22], and compare the search results and computation time of the traditional search methods with ours.

The rest of this paper is organized as follows. We briefly describe binary gravitational waves in Section 2. Section 3 introduces our search method and develops a way to accelerate the search. Moreover, we show our search results in Section 4. LISA's ability to detect the Milky Way structure is shown in Section 5. According to these search results, we give a suggested signal-to-noise ratio (SNR) threshold value in future actual space-based gravitational wave detection missions in Section 6. Finally, our conclusions are presented in Section 7.

II. LDC DATA DESCRIPTION

A. DWD binary gravitational wave

There are two double white dwarf (DWD) binaries in LDC1-4:

- (1) Detached DWD binaries. They only evolve with the release of orbital energy by GWs. There is no exchange of matter between the two stars [29, 30].
- (2) Interacting DWD binaries. When the binaries are close enough, two stars exchange matter [29, 30]. GWs and masses transfer affect the orbit together [31]. We currently have 22 known interacting binaries, AM CVn stars, with periods ranging from 5.4 to 65 minutes [32, 33].

DWD binaries gravitational waves in the source frame are defined as:

$$h_+(t) = \mathcal{A} (1 + \cos^2 \iota) \cos \Phi(t), \quad (1)$$

$$h_\times(t) = -2\mathcal{A} \cos \iota \sin \Phi(t), \quad (2)$$

$$\Phi(t) = \phi_0 + 2\pi f t + \pi \dot{f} t^2, \quad (3)$$

where \mathcal{A} represents the GW amplitude, ι represents the DWD binary orbit to the line of sight from the Solar System barycentric (SSB) origin, ϕ_0 represents the initial phase, f is the GW frequency, and \dot{f} is the first order derivative of f .

For detached DWD binaries, combining f with \dot{f} , we can obtain their chirp masses \mathcal{M} :

$$\dot{f} = \frac{96}{5} \pi^{8/3} \mathcal{M}^{5/3} f^{11/3}. \quad (4)$$

With GW amplitudes \mathcal{A} , the distances D between binary systems and solar can be calculated:

$$\mathcal{A} = \frac{2\mathcal{M}^{5/3} (\pi f)^{2/3}}{D}. \quad (5)$$

B. LISA response

LISA rotates around the sun with a cycle of one year, 20 degrees behind the Earth [34]. It has three satellites to form an equilateral triangle. Each side of the triangle is 2.5 million kilometres [2]. There are laser beams between each of the two satellites to measure the change in the distance between them. LISA will generate three separate pieces of data on three arms. Because the phase noise of the laser seriously pollutes the detection data, it must combine these data from different arms to reduce the impact of laser phase noise [35]. LDC1 uses the first-generation Time-delay interferometry (TDI) Michelson combinations denoted by X, Y, and Z. The first-generation TDI assumes the distances between spacecrafts are constant, just like a rigid body [36].

We use data streams whose characteristic is that instrumental noises are uncorrelated [24] by recombining the three channels XYZ into AET [35–37]:

$$\begin{aligned} A &= \frac{Z - X}{\sqrt{2}}, \\ E &= \frac{X - 2Y + Z}{\sqrt{6}}, \\ T &= \frac{X + Y + Z}{\sqrt{3}}. \end{aligned} \quad (6)$$

There are 29857650 DWD binaries in LDC1-4 data, adding stationary gaussian simulated instrumental noise.

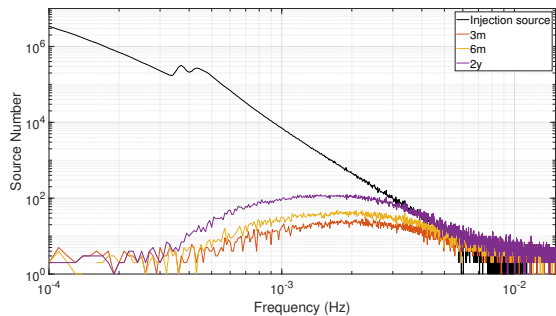


Figure 1. The black line presents the number of injection sources in LDC1-4 per frequency bin from 1×10^{-4} Hz to 1.5×10^{-2} Hz. The other three coloured lines represent the reported sources from direct-search to different data lengths. The number of accelerate-search to the two-year data reported sources (not shown in this figure) is the same as direct-search to the first three-month data. The width of each frequency bin is 0.01mHz.

Each series in LDC1-4 data is uniformly sampled every 15 seconds. The data is given by:

$$\bar{y}^I = \bar{S}^I + \bar{n}^I, \quad (7)$$

where \bar{S}^I denotes the collective GW signal from all the DWD binaries with $I \in \{A, E, T\}$, \bar{n}^I denotes the instrumental noise realization, and \bar{x} denotes a row vector. For LDC1-4 data, sampling number $N = 4194304$ corresponds to the observational time $T_{obs} = 2$ years. Each binary system is described by eight parameters, which are Frequency f , FrequencyDerivative \dot{f} , EclipticLatitude β , EclipticLongitude λ , Amplitude \mathcal{A} , Inclination ι , Polarization ψ and InitialPhase ϕ_0 . Almost all DWD binaries in LDC1-4 data have frequencies in the range of (0.1,15) mHz. The number of these sources overgrows as the frequency decreases, as shown in the solid black line in Fig. 1. The other lines present the number of reported sources in different frequency bins from three search situations.

The LISA orbital motion produces the Doppler effect. The earth moves around the sun at about 30 kilometres per second, and LISA has a similar speed. By the doppler effect formula, $f_1 = f \times \frac{c \pm v}{c}$ (c is the speed of light), the GW frequency will move $\approx 0.02\%$ of itself back and forth. It disperses the energy of the gravitational wave signal at a single frequency and overlaps signals with different frequencies, making the problem of resolving them more challenging. As LISA orientation changes, its sensitivity to different sky areas will change. For the same signal, its signal strength induced by LISA periodically changes with LISA sensitized in different directions, as shown in Fig. 2. In other words, a GW signal has different SNRs detected at different periods of one year.

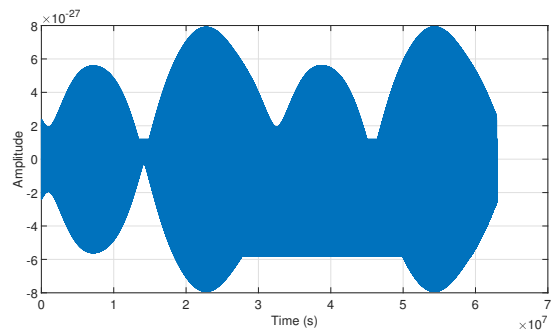


Figure 2. One DWD binary gravitational wave is modulated by LISA with a one-year periodicity. The data length is two years.

III. SEARCH METHOD

A. Search pipeline: GBSIEVER

A single DWD binary gravitational wave signal can be expressed as:

$$\bar{s}^I(\theta) = \bar{a}\mathbf{X}^I(\kappa), \quad (8)$$

where $\bar{a} = (a_1, a_2, a_3, a_4) \in R^4$ and $\mathbf{X}^I(\kappa)$ is a matrix of template waveforms. \bar{a} is the reparametrization of four extrinsic parameters \mathcal{A} , ϕ_0 , ψ and ι . $\mathbf{X}^I(\kappa)$ depends on the four remaining intrinsic parameters: f , \dot{f} , β and λ . GBSIEVER uses the \mathcal{F} -statistic proposed by Jaranowski in 1998 [38] to search for monochromatic gravitational waves. It maximizes the log-likelihood ratio $\log \Lambda$ (combining AET channels data) concerning parameters a_i , by solving:

$$\frac{\partial \log \Lambda}{\partial a_i} = 0. \quad (9)$$

Then it substitutes the maximum likelihood estimators \hat{a}_i in $\log \Lambda$ yielding the reduced log-likelihood ratio denoted by \mathcal{F} -statistic. In the intrinsic parameters search space, one finds the \mathcal{F} -statistic maximum and then obtains four extrinsic parameters through analytic expression (see [24] for more detail).

In GBSIEVER, the template waveforms are generated by using the expressions in Ref. [24], while the DWD binaries GW signals in LDC1-4 are generated by the FastGB code [39]. We have verified that they are in good agreement for the A and E combinations in the frequency range we are interested in. It divides GWs in the frequency range from 9×10^{-5} Hz to 1.501×10^{-2} Hz into 1491 frequency bins to search separately. The width of each bin is 2×10^{-5} Hz. There is a 50% overlap between two adjacent frequency bins. In each bin, considering spectrum leakage due to the Doppler effect, the Tukey window is used to weaken the effect of the edge of each frequency bin, and we take the results in the range with central 1×10^{-5} Hz (acceptance zone), as shown in

the black section of Fig. 4. We search each bin until it finds all GW signals with SNR less than 7 for five consecutive times. We refer to the GW parameter sets used to generate the LDC1-4 data as injection sources, and the acceptance zone search results come from GBSIEVER as reported sources.

Particle swarm optimization (PSO) [40] performs well in finding the optimal value of high-dimensional, nonlinear, and nonconvex optimization problems. It has been proven effective in previous experiments to obtain four intrinsic parameters of DWD binaries [22]. In GBSIEVER, 40 particles are randomly scattered in the 4-dimensional search space (f , \dot{f} , β and λ) and then we calculate the \mathcal{F} -statistic for each particle. The particles explore the search space randomly for better \mathcal{F} -statistic values following iterative rules. If a particle changes upon a good \mathcal{F} -statistic value, other particles eventually converge to its location and refine the \mathcal{F} -statistic value further. According to experience, it takes 2,000 iterations per search to ensure these particles converge. Every time a signal is found, it is removed from the original data, and we search for the next signal in the residual.

Cross-validation expands the search ranges for \dot{f} in the secondary run when $f \leq 4 \times 10^{-3}$ Hz. Comparing the search results in the primary run can eliminate some false sources in the low-frequency range and improve the detection rate. In this paper, our attention focused on confirmed sources screened by the correlation coefficient R (Section III C). Therefore, we did not use cross-validation in this paper.

Most of the search time is spent computing the \mathcal{F} -statistic. In particular, the longer the data length is, the more time it takes to calculate the \mathcal{F} -statistic for each particle in PSO. We refer to the method of searching directly with GBSIEVER as direct-search. We estimate that for direct-search to the two-year data of LDC1-4, already calculated in Ref. [22], it will take about 150 days to rerun it on the server we are currently using. More details on GBSIEVER can be found in Ref. [22].

B. Accelerate the individual detection process

The direct-search to the two-year data is time-consuming. Moreover, it is hard to imagine processing the data after LISA has completed all detection missions. We can start a search when LISA has been working for a while. It can be processed faster and is enough to reveal preliminary information about DWD binaries. (Results are shown in the section IV.)

We first direct-search to a short period of LDC1-4 data (such as the first three-month data), and then use f results from this, limit the search space of f in the following search (such as the two-year data). In GBSIEVER, the width of the frequency range of each bin is 0.02 mHz. For the first three-month data and the first six-month data, most report sources have absolute frequency errors $|\Delta f| \leq 1 \times 10^{-6}$ Hz (See Fig. 3). So we center

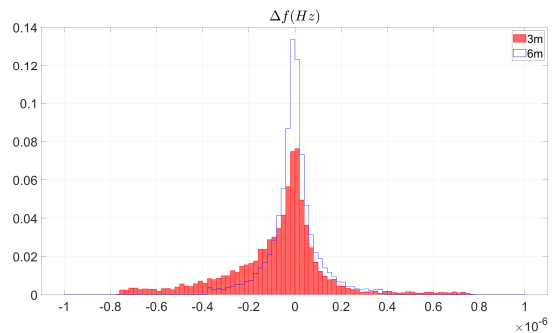


Figure 3. The red blocks and the blue line correspond to the absolute frequency error of direct-search to the first three-month data (3m) and the first six-month data (6m), respectively. Y-coordinate is the number of histograms to all reported sources ratio. Most errors are within the range $|\Delta f| \leq 1 \times 10^{-6}$ Hz. Based on this, we narrow the frequency search range in the following search and reduce the number of iterations.

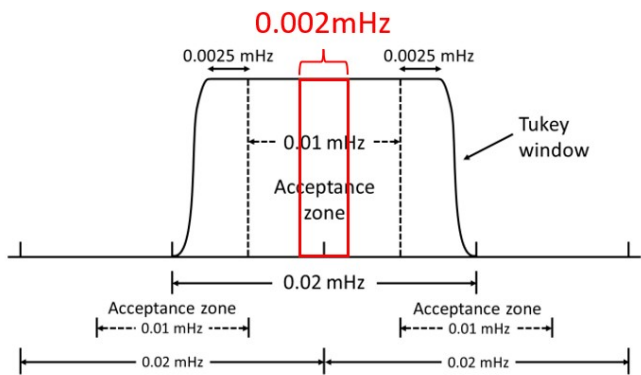


Figure 4. Direct-search using a Tukey window bandlimits the data in the Fourier domain to 0.02 mHz. Only the search results that belong to the central 0.01 mHz interval, called the acceptance zone, are retained as reported sources. The adjacent bin acceptance zone is contiguous. Accelerate-search uses the f results searched from the first three-month data, narrowing the f search range of the two-year data for each source from 0.02 mHz to 0.002 mHz.

on the f value from the direct-search to the first three-month data, extending it on both sides with 0.001 mHz, to obtain the new range of frequency in searching the two-year data whose width is 0.002 mHz (the red line in Fig. 4), which is one-tenth of the previous search space. As the search space decreases, it needs lower iterations for search points to converge. We reduced the number of iterations from 2000 to 400. Therefore the time spent per search was also reduced by five times. We call this method accelerate-search. It limits the number of reported sources in each frequency bin and narrows the frequency search range of each source based on reported sources from the direct-search to the first acquired data. In this paper, accelerate-search is based on the f results from direct-search to the first three-month data.

C. Detection Criteria

We have two criteria for judging the reliability of these reported sources. Firstly, we calculate their optimal SNR:

$$SNR = \sqrt{T \sum_I (\bar{s}^I(\theta') * \bar{s}^I(\theta')) / S_n^I(f)}, \quad (10)$$

where θ' represents reported source parameter sets. $I \in \{A, E, T\}$. $T = 15s$ represents the sampling interval. Because each DWD binary signal locates a tiny frequency band, the noise PSD $S_n(f)$ in this band is treated as a constant approximately.

In addition to the SNR, we also calculate the correlation coefficient R between the reported source parameter sets θ' and the injection source parameter sets θ to assess the similarity between their GW signal waveforms:

$$R(\theta, \theta') = \frac{C(\theta, \theta')}{[C(\theta, \theta)C(\theta', \theta')]^{1/2}}, \quad (11)$$

$$C(\theta, \theta') = \sum_I (\bar{s}^I(\theta) * \bar{s}^I(\theta')) / S_n^I(f).$$

We pick up parameter sets with $SNR \geq 3$ from all injection sources in two years of observation, as θ in Eq. 11. They named selected injection sources, and the number of them is 66696. Other injection sources with lower SNR are not considered to exist in our reported sources. For each reported source, the corresponding R takes the maximum value calculated with selected injection source parameter sets which have $\Delta f = |f(\theta) - f(\theta')| < 6/T_{obs}$. T_{obs} is the duration of detection. Generally, a reported source with $R \geq 0.9$ is seen as a confirmed source. And the reported source with $R < 0.9$ is seen as an unconfirmed source or a false source. The detection rate D of DWD is defined as the number of confirmed sources N_c relative to the reported sources N_r in one search, $D = N_c/N_r$ as did in previous literature [22] [41]. Fig. 5 shows the search diagram relating to the sources defined in this paper.

IV. SEARCH RESULTS

A. Source candidates

We directly search the first three-month data (3m), the first six-month data (6m) and the two-year data (2y), and apply the above proposed accelerating method to the two-year data (3m.2y) based on the results of direct-search to the first three-month data. Table I shows the computation time and the number of sources for each search situation. Computation time means the time it takes to conduct a complete search, and search efficiency is the normalized number of confirmed sources detected in a unit of time. The search efficiency of accelerate-search to the two-year data is twenty times as much as

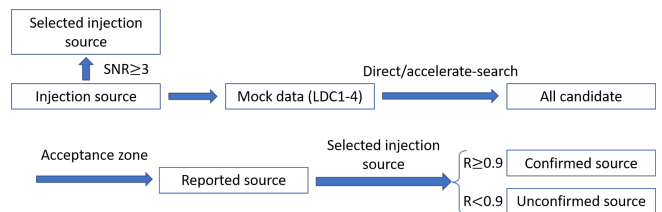


Figure 5. The search diagram in this paper. Injection sources are used to generate mock LISA data LDC1-4, among which $SNR \geq 3$ in two years of observation is the selected injection source. The candidates in the acceptance zone are reported sources. The correlation coefficient R of each reported source calculate with the selected injection sources. Moreover, the reported source with $R \geq 0.9$ is a confirmed source. Otherwise, it is considered an unconfirmed source. Detection rate D is the ratio of the confirmed sources number N_c to the reported sources number N_r . The results of those sources in different search strategies are shown in Tab. I.

that of direct-search to the two-year data. It is because accelerate-search has a lower number of iterations per search and uses less time for searching in low-frequency locations, where reported sources are often unconfirmed. Most reported sources with $f < 4 \times 10^{-3}$ Hz admit $R < 0.9$, which reduces the detection rate (compare Fig. 2 and Fig. 9). Direct-search to the two-year data has the most sources and consumes the longest computation time. It finds 37399 reported sources, with 13269 confirmed sources among them. This means the detection rate $D_{2y} = \frac{13269}{37399} = 35\%$. Accelerate-search to the two-year data has 11440 reported sources and 6651 confirmed sources, with a detection rate $D_{3m.2y} = \frac{6651}{11440} = 58\%$. The detection rates for the direct-search to the first three-month and the first six-month data are 27% and 31%, respectively. If we take the reported sources from direct-search to the two-year data as the standard, the normalized detection rate $D^n = N_c/N_r^{2y}$. The D_{3m}^n , D_{6m}^n , D_{2y}^n , $D_{3m.2y}^n$ are 8%, 15%, 35% and 18%, respectively. We take the computation time consumed in direct-search to the two-year data as a unit in Fig. 6. Therefore, the computation times (red line) for direct-search to the first-three month data and the first six-month data, accelerate-search to the two-year data are 0.016, 0.044, and 0.024, respectively. In the end, accelerate-search to the two-year data takes about one-fortieth time of direct-search to the two-year data to obtain about half the number of confirmed sources.

Fig. 7 shows the correlation coefficient R histogram distribution of the reported sources. A higher R value means the reported source is more similar to the injection source. The SNR histogram distribution of reported sources and confirmed sources are shown in Fig. 8(a) and Fig. 8(b). The confirmed sources in accelerate-search are the sub-population in direct-search with higher SNRs. A considerable proportion of reported sources from direct-search to the two-year data (2y) with $SNR \sim 10$ does not meet our screening criteria ($R \geq 0.9$), and it does not

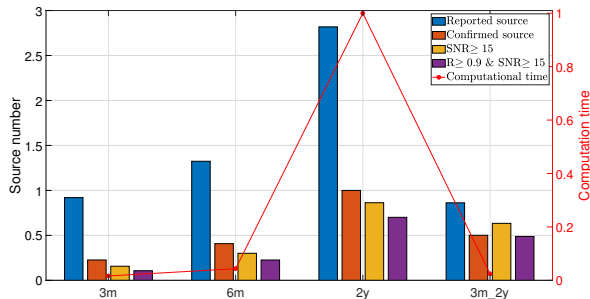


Figure 6. The figure visualizes the data in Tab. I. The left y-coordinate unit is the number of confirmed sources from the direct-search to the two-year data (2y). The right y-coordinate takes the computation time of direct-search to the two-year data as a unit.

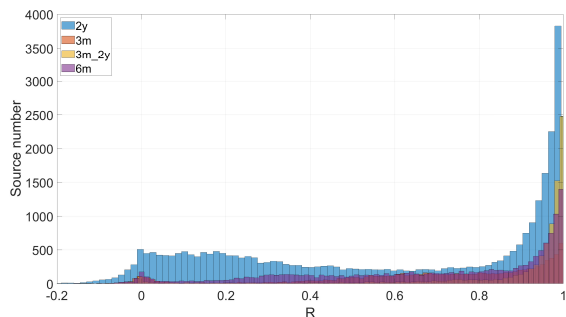


Figure 7. The histogram distribution of R of reported sources, which is obtained in four search situations.

belong to the list of confirmed sources. For space-based gravitational wave detection, source with $\text{SNR} \geq 15$ are usually selected as a reliable reported sources. Direct-search to the two-year data finds 11453 reported sources with $\text{SNR} \geq 15$, and the accelerate-search finds 8411 ones, which is 73% of the direct-search result. For those sources with $\text{SNR} \geq 20$, two search situations have a similar SNR histogram distribution. It means accelerate-search has a similar ability in searching for GW with a slightly bigger SNR. In actual GW detection, we cannot calculate R because the injection source parameter sets are unknown, so the main criterion is SNR. We checked out the reported sources that satisfy $R \geq 0.9$ and $\text{SNR} \geq 15$. The higher the proportion of these sources in $\text{SNR} \geq 15$, the better $\text{SNR} \geq 15$ as the criterion for LISA to detect DWD binaries GWs. For the direct-search to the first three-month data, the first six-month data, the two-year data, and the accelerate-search to the two-year data, the proportion is 68%, 75%, 81%, and 77%, respectively. Fig. 9 shows the number of confirmed sources in different frequency bins from four search situations. When the frequency f is lower than 4×10^{-3} Hz, the search capability decreases. Moreover, it cannot even search for some confirmed sources at a frequency below 1×10^{-3} Hz.

B. Residual data

We calculate the LISA response signals of all confirmed sources in four search situations and subtract these signals from the LDC1-4 TDI A data to obtain the residual data. Fig. 10 compares the LDC1-4 data power spectral densities (PSDs), the residuals PSDs and the instrumental noise PSDs in different search situations. The time length of LDC data and noise is consistent with that of the residual. In space-based gravitational wave detection, DWD binary signals in the Milky Way constitute a strong foreground noise. With the increase in data length, more confirmed sources were found, and the residual of DWD binary signals is more similar to LISA instrumental noise. However, confirmed sources are mainly concentrated in the high-frequency domain ($f \geq 4 \times 10^{-3}$ Hz) and the medium-frequency domain (1×10^{-3} Hz $\leq f < 4 \times 10^{-3}$ Hz). In the low-frequency domain ($f < 1 \times 10^{-3}$ Hz), there is little difference in the residuals obtained in the four search situations. Comparing the direct-search and the accelerate-search to the two-year data, the main difference between their residuals is because three-month data is too short, so the search cut-off according to $\text{SNR} \geq 7$ miss some signals, which limits the search number in accelerate-search to the two-year data. Suppose we use longer data search results, such as the direct-search to the first six-month data, which has 17571 reported sources. We can theoretically have more confirmed sources for accelerate-search to the two-year data, and its residual PSD will be more similar to the residual PSD of direct-search to the two-year data.

1. MBHB's SNR

We use LDC1-1 data, the LISA response signal of a single gravitational wave generated by a massive black hole binary (MBHB), to test the influence of different noise assumptions on MBHB's SNR. The two black hole detector frame masses are $2.8 \times 10^5 M_\odot$ and $2.8 \times 10^6 M_\odot$, and their redshift $z = 6.1$. LDC1-1 sample frequency is 1/10, and we interpolate its signal at a sampling frequency of 1/15, which is consistent with LDC1-4. The signal length of LDC1-1 is 1.33 years. We calculate the SNR of MBHB by:

$$\text{SNR} = \left| \sqrt{\sum \frac{1}{N f_s} (\tilde{h}_{MBHB} / \tilde{S}_n) \tilde{h}_{MBHB}^\dagger} \right|, \quad (12)$$

where N is the sampling number and f_s is the sampling frequency. \tilde{h}_{MBHB} represents the discrete Fourier transform (DFT) of time-domain signal h_{MBHB} in LDC1-1. \dagger is a transposed conjugate symbol. And \tilde{S}_n represents the PSD with different noise assumptions. All calculations are based on the TDI A. Tab. II presents the SNR for this MBHB signal on different noise assumptions, which are LISA instrumental noise, LDC1-4 data, and residuals from four search situations (Fig. 10). It can

	Computation time (s)	All candidate	Reported source (N_r)	Confirmed source (N_c)	Detection rate (D)	Search efficiency	$SNR \geq 15$	$R \geq 0.9$ & $SNR \geq 15$
3m	222,806	20737	12,213	3010	27%	13.79	2085	1424
6m	590,209	30220	17,571	5418	31%	9.37	3993	3004
2y	13,525,967	100783	37,399	13269	35%	1.00	11453	9300
3m_2y	327,818	12213	11,440	6651	58%	20.70	8411	6477

Table I. This table shows the source number of direct-search to the first three-month data, the first six-month data, the two-year data, and accelerate-search to the two-year data, as well as their computation time. All source contains search results that are not in the acceptance zone. We take the search efficiency of direct-search to the two-year data as the unit.

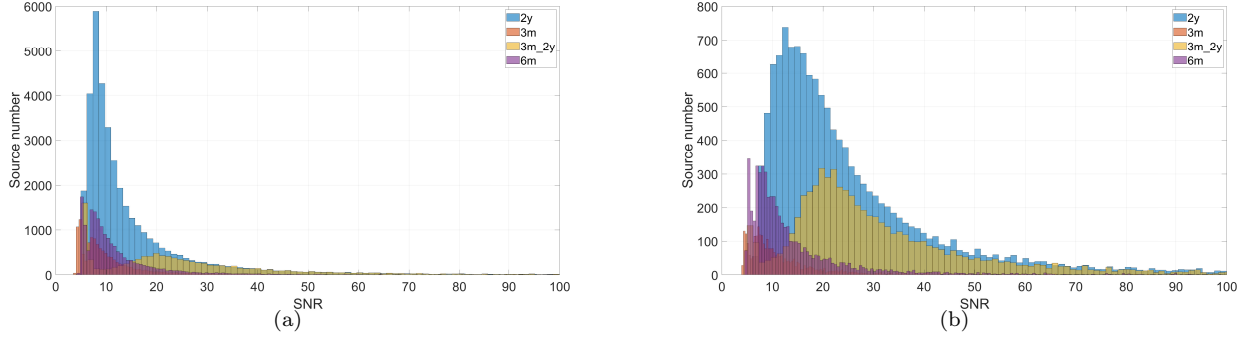


Figure 8. The histogram distribution of SNR of reported sources (Fig. 8(a)), and confirmed sources (Fig. 8(b)).

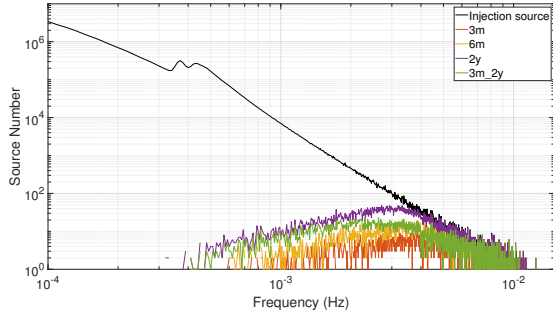


Figure 9. The black line has the same SNR meaning as Fig. 1. The other four colored lines represent all confirmed sources obtained by four search situations. The width of each frequency bin is 0.01mHz.

be seen that the foreground noise from DWD binaries does not significantly affect the SNR of the MBHB signal. Fig. 11 shows the MBHB signal, confirmed sources with two search situations, and the LISA sensitivity curve from Ref. [42], which is consistent with LISA instrumental noise. The vertical coordinate is dimensionless [43]. Rather than plotting the signal directly, it often plots $h_{eff}^2 = 16f(2fT)S_h(f)/5$ to account for the influence of coherent signal extraction [42]. Accelerate-search to the two-year data has fewer confirmed sources than direct-search to the two-year data. The missing parts are the blue dots whose characteristic strains are closer to the LISA sensitivity curve, which means they have a lower SNR.

2. Contamination effects on the subtraction of DWDs

Inaccurate subtraction of individual DWD can lead to contamination on the residual data that becomes more pronounced as detection continues. We explore this effect by a case study, using a frequency bin ranging from 4.18×10^{-3} Hz to 4.20×10^{-3} Hz (the 410th bin in our data). To evaluate the impact of inaccurate detections, we consider reported sources as “inaccurate” sources, while injection sources were deemed “accurate”. The A channel data is used to show this effect:

$$\begin{aligned} \bar{r}_{inj-t}^A &= \bar{y}_t^A - \bar{s}_{inj-t}^A, \\ \bar{r}_{rep(K)-t}^A &= \bar{y}_t^A - \bar{s}_{rep(K)-t}^A, \end{aligned} \quad (13)$$

where \bar{r}^A is the residuals in the A channel, \bar{s}^A is the GWs signals come from injection or reported sources. We consider the first three-month ($t = 3m$) and the two-year ($t = 2y$) data, and compare the reported sources from direct-search to the first three-months data ($K = 3m$) and the two-year data ($K = 2y$), and accelerate-search to the two-year data ($K = 3m_2y$).

By comparing the power spectral densities (PSDs) of the residuals \bar{r}_{inj-t}^A and $\bar{r}_{rep(K)-t}^A$, we can assess the extent of the inaccurate subtracted contamination. We plot the PSDs of the residuals $\bar{r}_{inj-2y}^A, \bar{r}_{rep(2y)-2y}^A, \bar{r}_{rep(3m_2y)-2y}^A, \bar{r}_{inj-3m}^A, \bar{r}_{rep(3m)-3m}^A, \bar{r}_{inj-6m}^A, \bar{r}_{rep(6m)-6m}^A$ of the 410th frequency bin in Fig. 12(a) – Fig. 12(c), alongside the corresponding subtracted sources whose SNRs calculated by Eq. 10.

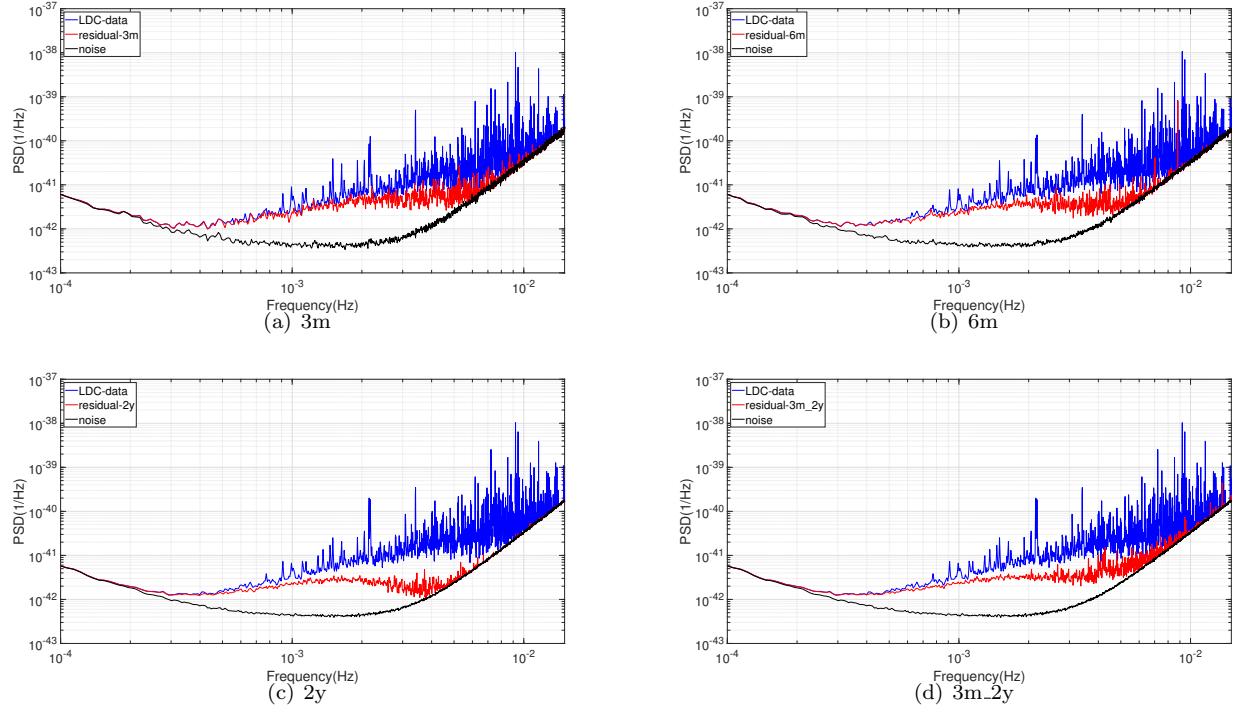


Figure 10. These figures show the PSD comparison of the LDC1-4 data, the residuals from four search situations, and the LISA instrumental noise. The noise and data length is the same as the residual. All data is calculated on the TDI A.

	Instrument noise	LDC1-4	2y-residual	3m_2y-residual
MBHB	135.7084	99.7673	121.3335	112.0379

Table II. For a certain MBHB signal, SNR is obtained under different noise assumptions. The different noise assumptions do not have a tremendous influence on the MBHB's SNR.

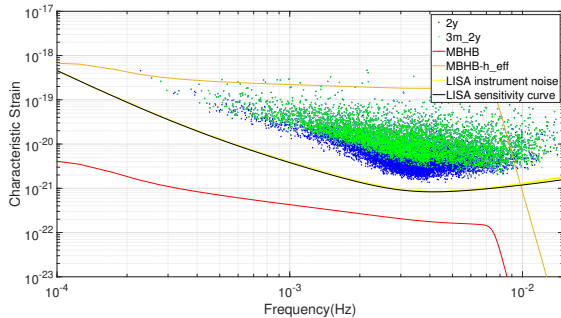


Figure 11. The blue and green points correspond to confirmed sources from direct-search and accelerate-search to the two-year data, respectively. The LISA sensitivity curve is consistent with mock LISA instrumental noise. And the MBHB signal comes from LDC1-1 data, whose detector frame masses are $2.8 \times 10^5 M_\odot$ and $2.8 \times 10^6 M_\odot$.

A larger area ($\int |S_{\bar{r}A}^{inj-t}(f) - S_{\bar{r}A}^{rep(K)-t}(f)|df$) between two PSDs indicates a greater contamination effect from reported (inaccurate) sources. These areas have been

colored in Fig. 12(a) – Fig. 12(c). For the case study in the 410th frequency bin, we subtract 1, 10, and 15 sources, respectively, resulting in areas of 1.72×10^{-49} , 9.49×10^{-48} , 1.42×10^{-47} for $K = t = 2y$, and 2.24×10^{-49} , 4.90×10^{-48} , 7.03×10^{-48} for $K = 3m_2y$, $t = 2y$, and 2.17×10^{-47} , 3.76×10^{-47} , 4.78×10^{-47} for $K = t = 3m$, and 3.21×10^{-48} , 2.02×10^{-47} , 2.00×10^{-47} for $K = t = 6m$. As the number (N) of subtracted sources increases, the areas grow larger, indicating a more significant contamination effect from reported (inaccurate) sources.

We conduct the same process in two additional frequency bins, the 91st frequency bin (9.90×10^{-4} Hz– 1.01×10^{-3} Hz) and the 291st frequency bin (2.99×10^{-3} Hz– 3.01×10^{-3} Hz). Then we plot the trend of areas (Fig. 12(d)), which takes the $\int |S_{\bar{r}A}^{inj-2y}(f) - S_{\bar{r}A}^{rep(2y)-2y}(f)|df$ as unit one:

$$p = \frac{\int |S_{\bar{r}A}^{inj-t}(f) - S_{\bar{r}A}^{rep(K)-t}(f)|df}{\int |S_{\bar{r}A}^{inj-2y}(f) - S_{\bar{r}A}^{rep(2y)-2y}(f)|df}. \quad (14)$$

The number of subtracted sources are 1, 5, 10, and 15, respectively. In Fig. 12(d), the p value is higher when we

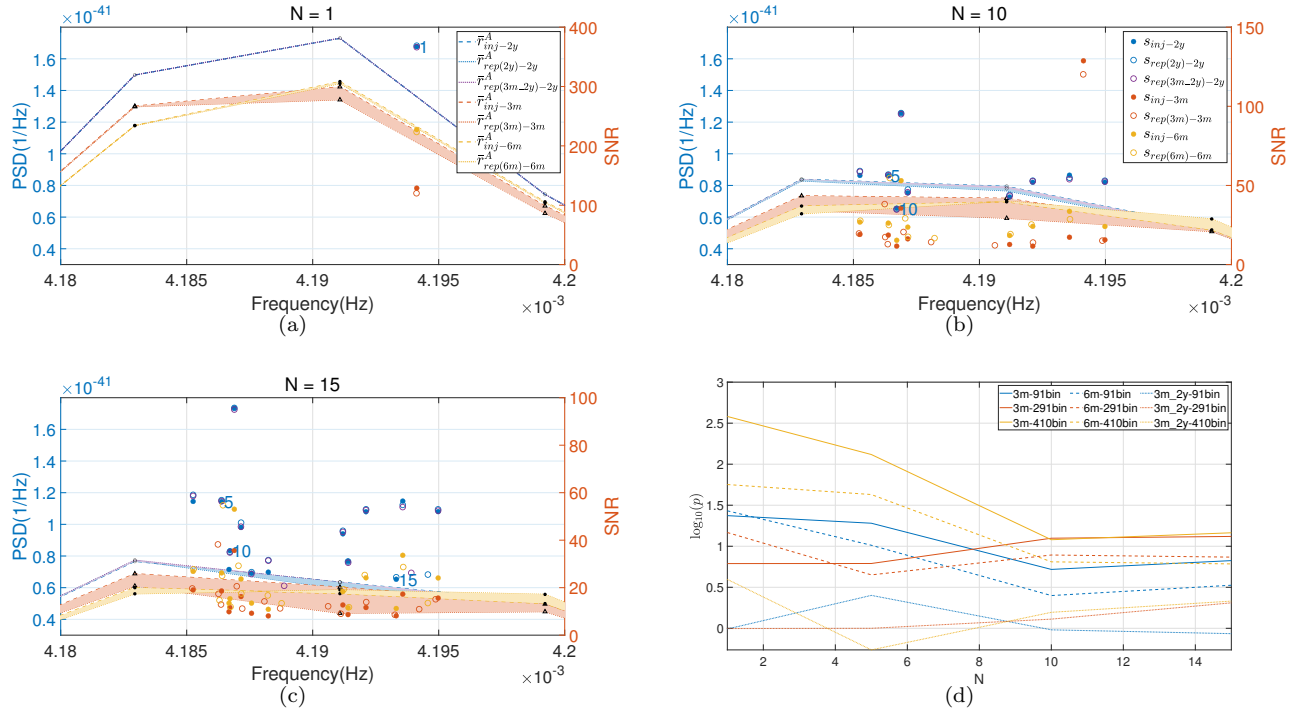


Figure 12. Figures 12(a), 12(b), and 12(c) display the PSDs of residuals \bar{r}_{inj-t}^A and $\bar{r}_{rep(K)-t}^A$, and their corresponding subtracted sources whose SNR calculated by Eq. 10 for the 410th bin in our data. The title indicates the number of subtracted sources (N), and the right y-axis corresponds to their SNRs. In each figure, the larger area ($\int |S_{\bar{r}_{inj-t}^A}(f) - S_{\bar{r}_{rep(K)-t}^A}(f)|df$) between the lines of the same t is, the greater impact of the contamination caused by inaccurate subtraction. Figure 12(d) shows the trend of areas (Eq. 14) which take the $\int |S_{\bar{r}_{inj-t}^A}(f) - S_{\bar{r}_{rep(2y)-2y}^A}(f)|df$ as unit one with the number of subtracted sources increases, and includes case studies in the 91st frequency bin (9.90×10^{-4} Hz – 1.01×10^{-3} Hz) and the 291st frequency bin (2.99×10^{-3} Hz – 3.01×10^{-3} Hz). We have marked the order of subtraction (1, 5, 10, 15) of the sources s_{inj-2y} .

use the shorter data length, such as 3m and 6m. This is because the shorter data has a greater potential for inaccurate removal of sources compared to the longer data, resulting in more contamination on the residual, which may lead to fewer confirmed sources when search the shorter data.

We repeated the same process for DWD as we did for MBHB. We calculate the SNR for the brightest injection source in each frequency bin in the A channel by Eq. 10, based on various noise assumptions: LISA instrumental noise, LDC1-4 data, and residuals from two search situations (Fig. 10). The SNRs are presented in the Tab. III. Due to the monochromatic nature of DWDs, they are more sensitive to noise at a single frequency. As a result, different noise assumptions can have a greater impact on the SNR of DWDs compared to that of MBHBs. The SNRs of a DWD can differ by a factor of 5 to 9 under two noise assumptions of instrumental noise or LDC1-4 data. This highlights the potential for subtracting out bright DWDs to enhance the detection sensitivity for weaker ones when searching in a specific frequency bin.

The impact of contamination on the accuracy of the next subtracted source's parameters is a complex issue. In this study, we present the four intrinsic pa-

rameter ($f, \dot{f}, \beta, \lambda$) accuracies for the next reported sources (2, 6, 11, 16) based on the respective areas ($\int |S_{\bar{r}_{inj-t}^A}(f) - S_{\bar{r}_{rep(K)-t}^A}(f)|df$) obtained from subtracting 1, 5, 10, 15 sources in three frequency bins. To ensure that the data length does not affect the parameters' accuracy, we only consider $t = 2y$ and $K = 2y \& 3m.2y$. In Fig. 13, the diameter of the circle represents the area value obtained by subtracting all preceding sources (1, 5, 10, 15). While the areas increase as the number (N) of subtracted sources grows, the parameter relative error has no clear correspondence with N . This indicate that the accuracy of estimated source parameters may be influenced by multiple factors, such as the SNR of the source itself, the distance in parameter space between this source and other subtracted sources, the density of all sources distribution in the frequency bin, and the bin in which this source resides. Further studies are needed to fully understand these factors.

C. Detection parameter error

What are the errors between confirmed source parameters and their corresponding injection source param-

	Instrument noise	LDC1-4	2y-residual	3m_2y-residual
91bin	58.9001	11.7234	18.0358	17.7068
291bin	62.5891	10.9944	28.2086	21.3617
410bin	264.4705	31.2997	138.5068	92.9885

Table III. For the brightest DWD source in each bin, SNRs are obtained in the A channel under different noise assumptions. The influence of different noise assumptions on the SNR of DWD is much greater than that of MBHB.

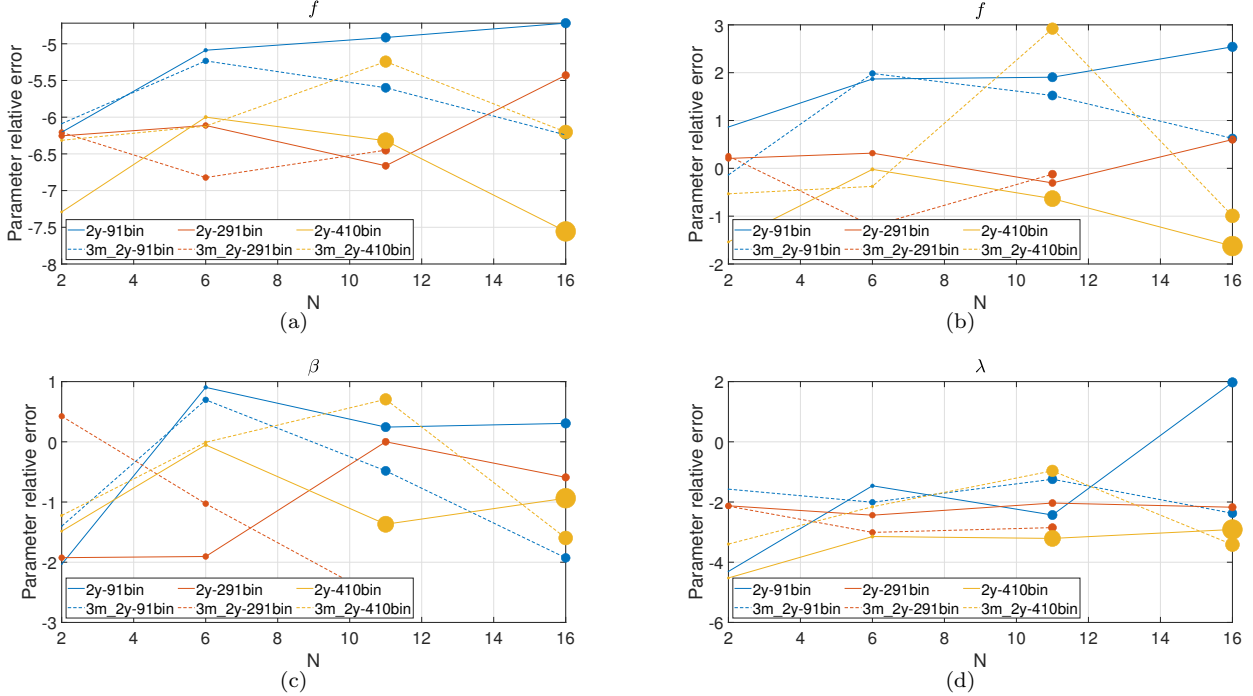


Figure 13. The X-axis represents the number (N) of subtracted sources, and the Y-axis represents the four intrinsic parameter (f , \dot{f} , β , λ) relative error in logarithmic base 10. The diameter of each circle represents the area value obtained by subtracting all preceding sources (1, 5, 10, 15). To display the area value, we use 1×10^{-51} as unit one and take the square root to obtain the diameter of the circle. For example, the circle in “3m_2y-410bin, $N=16$ ” has an area value of 1.42×10^{-47} , and its diameter is $\sqrt{\frac{1.42 \times 10^{-47}}{1 \times 10^{-51}}} \approx 119$.)

ters? Fig. 14 shows the absolute error histogram distribution of four intrinsic parameters for confirmed sources in direct-search to the two-year data and accelerate-search to the two-year data. In direct-search to the two-year data, the fraction of $|\Delta f| \leq 0.5 \times 10^{-8}$ Hz is 86.4%, the fraction of $|\Delta \dot{f}| \leq 2.5 \times 10^{-16} Hz^{-1}$ is 96.3%, the fraction of $|\Delta \beta| \leq 0.1$ rad is 87.5%, and the fraction of $|\Delta \lambda| \leq 0.05$ rad is 91.9%. In accelerate-search to the two-year data, the fraction of $|\Delta f| \leq 0.5 \times 10^{-8}$ Hz is 87.5%, the fraction of $|\Delta \dot{f}| \leq 2.5 \times 10^{-16} Hz^{-1}$ is 96.0%, the fraction of $|\Delta \beta| \leq 0.1$ rad is 91.7%, and the fraction of $|\Delta \lambda| \leq 0.05$ rad is 92.4%. Note that, although the fraction of $|\Delta f| \leq 0.5 \times 10^{-8}$ Hz in accelerate-search is slightly larger than in direct-search, the confirmed sources in accelerate-search are the sub-population in direct-search with higher SNRs as shown in Fig. 8(b).

V. LISA’S ABILITY TO DETECT THE MILKY WAY STRUCTURE

A. Source distribution in ecliptic coordinate system

LISA’s detecting gravitational waves generated by DWD binaries in the Milky Way may be a powerful astronomical tool [44–49]. Specifically, we use the above confirmed sources to discuss the possible research of the Milky Way structure through LISA. Fig. 15 presents the distribution of confirmed sources in the ecliptic coordinate system. Kernel density estimation is used to estimate the density of confirmed sources per square degree of sky. Most sources are centered at the galactic center. We draw three contour lines from high to low density that account for different proportions of all confirmed sources, 10%, 50%, and 90%, respectively. Fig. 15(a) shows the

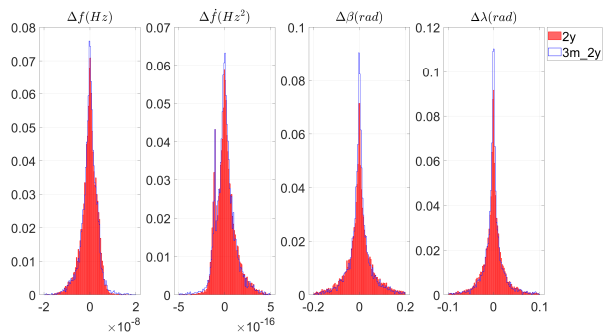


Figure 14. The absolute error histogram for four intrinsic parameters was obtained from direct-search and accelerate-search to the two-year data. The red zone represents direct-search, and the blue line represents accelerate-search. The second histogram has a bimodality due to some sources with $f \leq 1 \times 10^{-3}$ Hz has \dot{f} fall on the negative boundary of the search range, making they have a similar absolute error with -1×10^{-16} .

result of direct-search to the first three-month data, the top 10% region enclosed by the red circle corresponds to the density more than 1.3 sources per square degree, and the top 50% more than 0.4. Fig. 15(b) shows the result of direct-search to the first six-month data, the top 10% region corresponds to the density more than 4.2 sources per square degree, and the top 50% more than 1.3. Fig. 15(c) shows the result of direct-search to the two-year data, the top 10% region corresponds to the density more than 22.2 sources per square degree, and the top 50% more than 6.1. Fig. 15(d) shows the result of accelerate-search to the two-year data, the top 10% region corresponds to the density more than 7.7 sources per square degree, and the top 50% more than 1.9. All of the confirmed sources from the direct-search to the first three-month data and the first six-month data are scattered in the sky. This is because their data is not long enough, which enlarges the position error of LISA for each DWD binary. However, both direct-search and accelerate-search to the two-year data have less position error. Their average latitude error is about 2.3° , and the average longitude error is about 1.6° . When we only consider sources with $f \geq 4 \times 10^{-3}$ Hz, the average latitude and longitude error are 1.3° and 0.3° , respectively.

B. Source distribution in galactic coordinate system

It is assumed that all confirmed sources with $\dot{f} \geq 0$ come from DWD binary systems without mass transfer. Therefore, the distances D and chirp masses \mathcal{M} of DWD binaries can be calculated by Eqs. (4) and (5). With the known distance, we convert the source distribution in ecliptic coordinate system to that in galactic coordinate system and plot the density distribution of DWD binaries on the galactic disk. We also use kernel density estima-

tion to access the number of DWD binaries per square thousand light years. In fact, we have ignored the thickness of the galactic disk. Fig. 16 shows the DWD binaries distribution of four situations, and the location of the sun and the Galactic center. Fig. 16(a) shows all injection sources with $\dot{f} \geq 0$, whose number is 26433149, forming a disk with a radius of about 60,000 light years (~ 18 kpc). In the top 10% density region, there are more than 7413.1 DWD binaries per square thousand light years, and the top 50% more than 426.6. The density decreases with the increase of distance between the source and the galactic center. Fig. 16(b) presents the selected injection sources with $\dot{f} \geq 0$, whose number is 65510. All selected injection sources were selected by $\text{SNR} \geq 3$ for LISA over two years of observation. These sources are expected to have $\text{SNR} \geq 6$ during the four years of LISA observation. In the top 10% density region, there are more than 50.1 DWD binaries per square thousand light years, and the top 50% more than 14.1. The densest parts are concentrated near the solar system and the galactic center. We expect to eventually search all of these selected injection sources throughout the life of LISA. Fig. 16(c) presents confirmed sources with $\dot{f} \geq 0$ from the direct-search to the two-year data, whose number is 9927. In the top 10% density region, there are more than 10.5 DWD binaries per square thousand light years, and the top 50% more than 4.4. These sources are centralized on the sun-galactic center line, which we think is related to the direction of LISA's sensitivity. Fig. 16(d) presents all confirmed sources with $\dot{f} \geq 0$ from the accelerate-search to the two-year data, whose number is 5205. In the top 10% density region, there are more than 7.1 DWD binaries per square thousand light years, and the top 50% more than 3.9. Accelerate-search to the two-year data is less capable of detecting sources on the other side of the Galactic center than direct-search to the two-year data because they are so far away and tend to be accompanied by a lower SNR.

C. Distance and chirp mass error

Fig. 17 shows the relative error of distance and chirp mass for direct-search and accelerate-search to the two-year data. The x-axis is the distance between the source and the sun. The y-axis is $|\frac{\Delta\mathcal{M}}{\mathcal{M}_{inj}}|$ or $|\frac{\Delta D}{D_{inj}}|$, where $\Delta\mathcal{M} = |\mathcal{M}_{injection} - \mathcal{M}_{confirmed}|$ and $\Delta D = |D_{injection} - D_{confirmed}|$. For the sources with high frequency ($f \geq 4 \times 10^{-3}$ Hz), the relative error of the average chirp mass and distance in the direct-search are 14.5% and 28.2%, respectively, and the accelerate-search 12.0% and 24.0%. Sources with medium frequency (1×10^{-3} Hz $\leq f < 4 \times 10^{-3}$ Hz) have a relatively poor performance in parameters estimation. The relative error of the average chirp mass and distance in the direct-search are respectively 145.7% and 392.0%, and the accelerate-search 124.4% and 359.3%. Sources with the low-frequency

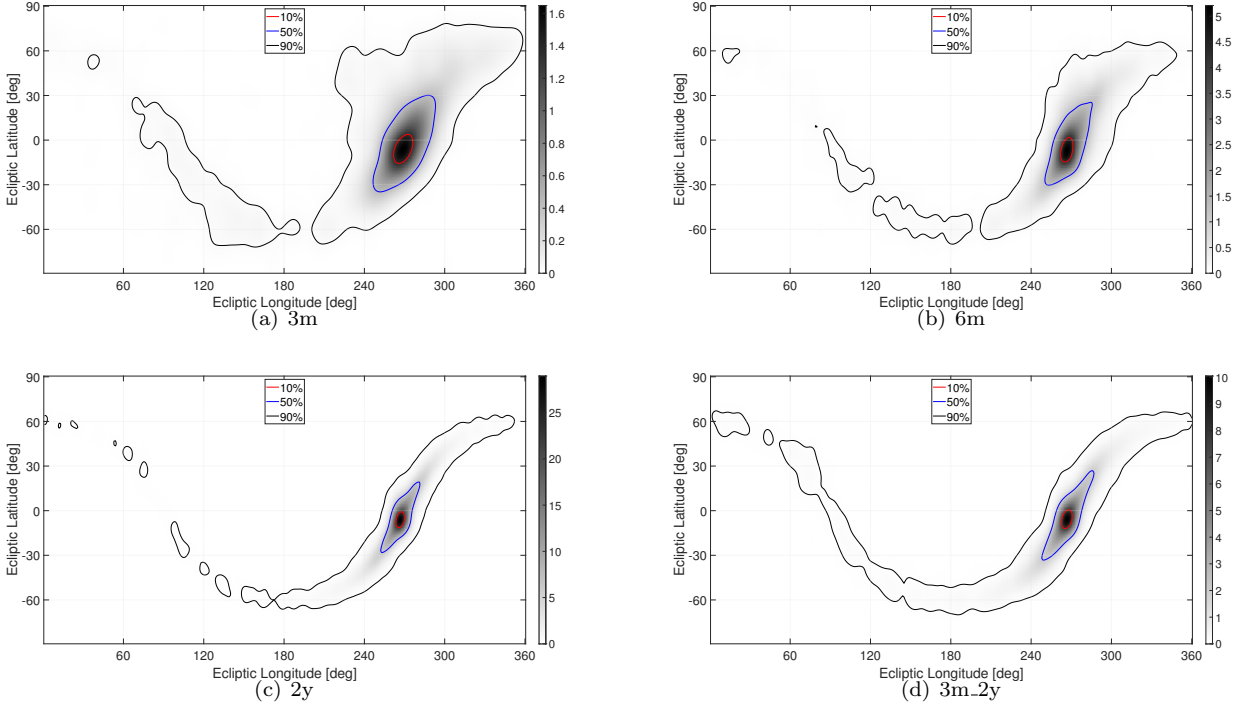


Figure 15. The distribution of confirmed sources in the ecliptic coordinate system. According to the number of sources per square degree, the sky is divided into several areas. Specifically, the red, blue and black lines represent the boundaries of the top 10%, 50% and 90% distribution area of all confirmed sources, respectively.

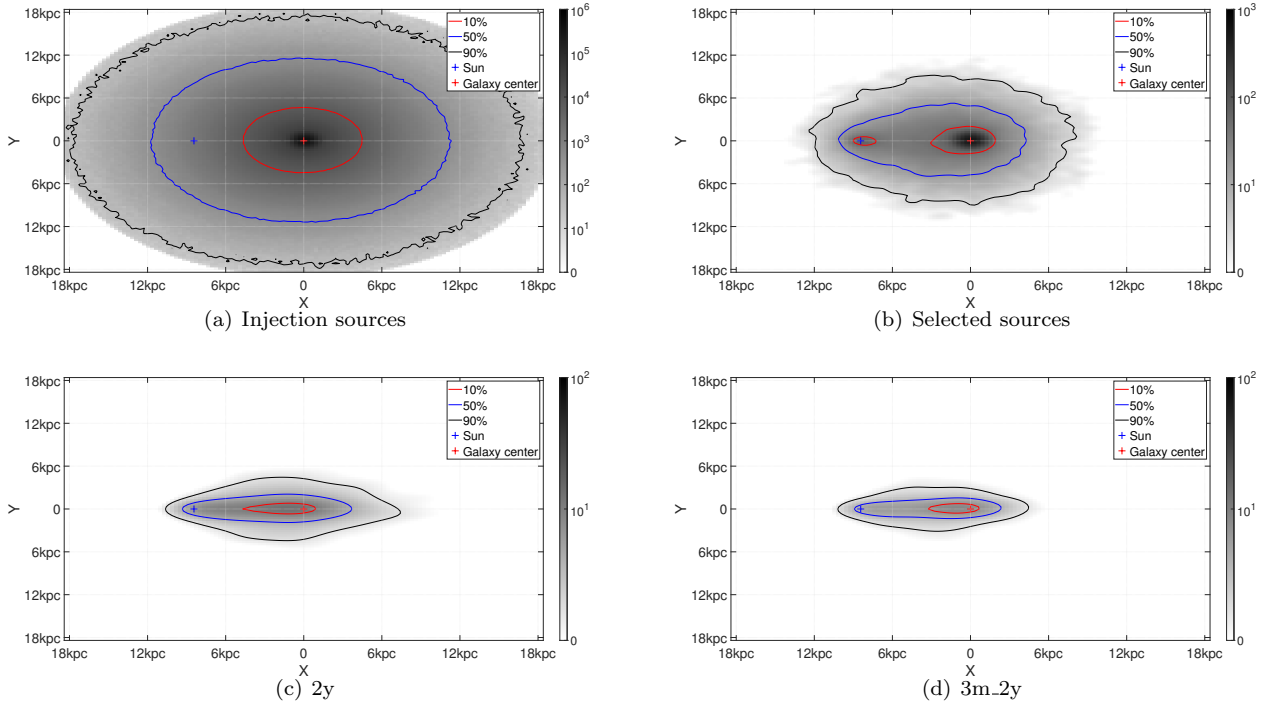


Figure 16. The distribution of confirmed sources with $\hat{f} \geq 0$ in the galactic coordinate system. The view is equivalent to looking down at the entire disk from the galactic north pole. The thickness of the disk is not shown. The color indicates the number of sources per square thousand light years. The red, blue and black lines represent the top 10%, 50% and 90% distribution area of all confirmed sources, respectively.

		R	
		≥ 0.9	< 0.9
SNR	$\geq \eta$	TP	FN
	$< \eta$	FP	TN

Table IV. All reported sources can be divided into four parts using R and SNR. There are true positive, false positive, false negative, and true negative.

range ($f < 1 \times 10^{-3}$ Hz) have the worst accuracy in parameters estimation. In general, for the two-year data, the direct-search is not as good as the accelerate-search in the estimation of distance and chirp mass.

VI. THE DETECTION SNR THRESHOLD

In realistic space-based gravitational wave detection, we cannot calculate R for reported sources because of the unknown injection source parameter sets. The main evidence to determine whether a DWD reported source is a real signal is its SNR. Being targeted at finding the sources confirmed with $R \geq 0.9$ in Sec. IV as much as possible, we try to seek out the best SNR threshold for searching DWD binary with LISA.

We take confirmed sources as the standard answer, using the Receiver Operating Characteristic Curve (ROC) to discuss the relation between SNR and R through four search results. In Tab. IV, R takes 0.9 as the threshold, and the SNR threshold η is a positive integer ranging from 7 to 21. We grouped all reporting sources into four categories. True Positive (TP) represents the reported source that both SNR and R are greater than the threshold. False Negative (FN) represents the reported source that meets $\text{SNR} \geq \eta$ and $R < 0.9$. False Positive (FP) represents the reported source that meets $\text{SNR} < \eta$ and $R \geq 0.9$. True Negative (TN) represents the reported source that both SNR and R are smaller than their threshold. Eqs. (15) and (16) mean the detection ability (DB) and the false alarm rate (FAR) when we determine the threshold η of SNR. That is the proportion of reported sources of $\text{SNR} \geq \eta$ to the confirmed sources, and the proportion of reported sources of $\text{SNR} \geq \eta$ to the unconfirmed sources. The larger the DB is, as long as the smaller the FAR is, the closer the results of the SNR screening and R screening is. That is to say, a larger DB and a smaller FAR corresponds to a better SNR threshold.

$$DB = \frac{TP}{TP + FP}, \quad (15)$$

$$FAR = \frac{FP}{FN + TP}. \quad (16)$$

Fig. 18 presents the ROC diagram in different frequency ranges. The lower SNR threshold will lead to

a higher DB but bring a bigger FAR problem. Moreover, the higher SNR threshold leads to a lower FAR and a lower DB. Therefore, finding a proper SNR threshold to balance the DB and FAR seems complicated. For direct-search situations, the longer the detection time, the closer the search results screened out by the SNR to the confirmed sources screened out by the R (closer to the upper left corner in the figure). In the case of accelerate-search to the two-year data, the overall DB is higher than the other three cases because it shields a lot of unconfirmed sources ($R < 0.9$) in the low and medium-frequency domain ($f < 4 \times 10^{-3}$ Hz). However, its FAR is also high, mainly because the number of unconfirmed sources is smaller than that of other cases (as can be seen from the fourth line in Tab. I), and the denominator in Eq. (16) is small, which makes a big FAR.

Fig. 18(a) contains the data in all frequency domains (1×10^{-4} Hz– 1.5×10^{-2} Hz). Taking the result of direct-search to the two-year data for an example (the red line), when the SNR threshold $\eta = 15$, the FPR is lower than 0.1, and the TPR is about 0.7. The ROC diagram in Fig. 18(b) corresponds the data in low and medium-frequency domains (1×10^{-4} Hz– 4×10^{-3} Hz). For the result of direct-search to two-year data, when the SNR threshold $\eta = 16$, the FPR is lower than 0.1, and the TPR is about 0.63. Fig. 18(c) is the ROC diagram corresponding to the data in high-frequency domains (4×10^{-3} Hz– 1.5×10^{-2} Hz). For the result of direct-search to two-year data, when the SNR threshold $\eta = 9$, the FPR is lower than 0.1, and the TPR is about 0.98. As shown in Fig. 19, based on the result of direct-search to the two-year data, the red line denotes the residual of the confirmed source, and the green line is the residual of the source screened by $\text{SNR} \geq 15$ throughout the frequency domain. The blue line represents the residual of the source screened by $\text{SNR} \geq 16$ in the low and medium-frequency domains and $\text{SNR} \geq 9$ in the high-frequency domains. There is a slight difference between the second type source (green line) and the third type source (blue line) on the high-frequency domains. The blue line almost coincides with the instrument noise curve, while the green line has many small bumps.

VII. CONCLUSIONS

An accelerated search method is proposed depending on the early search results from the previous LISA data. We demonstrate this approach with the GB-SIEVER method. For the LDC1-4 two year data, this accelerate-search strategy obtains about half of the confirmed sources within one-fortieth time of direct-search (Fig. 6), and almost identical parameter estimation on intrinsic parameters (f , \dot{f} , β and λ) (Fig. 14).

To verify the DWD binaries' foreground noise effect when searching for other types of sources, we calculate the SNR of the MBHB signal from LDC1-1 data ($m_1 = 2.8 \times 10^5 M_\odot$, $m_2 = 2.8 \times 10^6 M_\odot$, $z = 6.1$ and 1.33 years

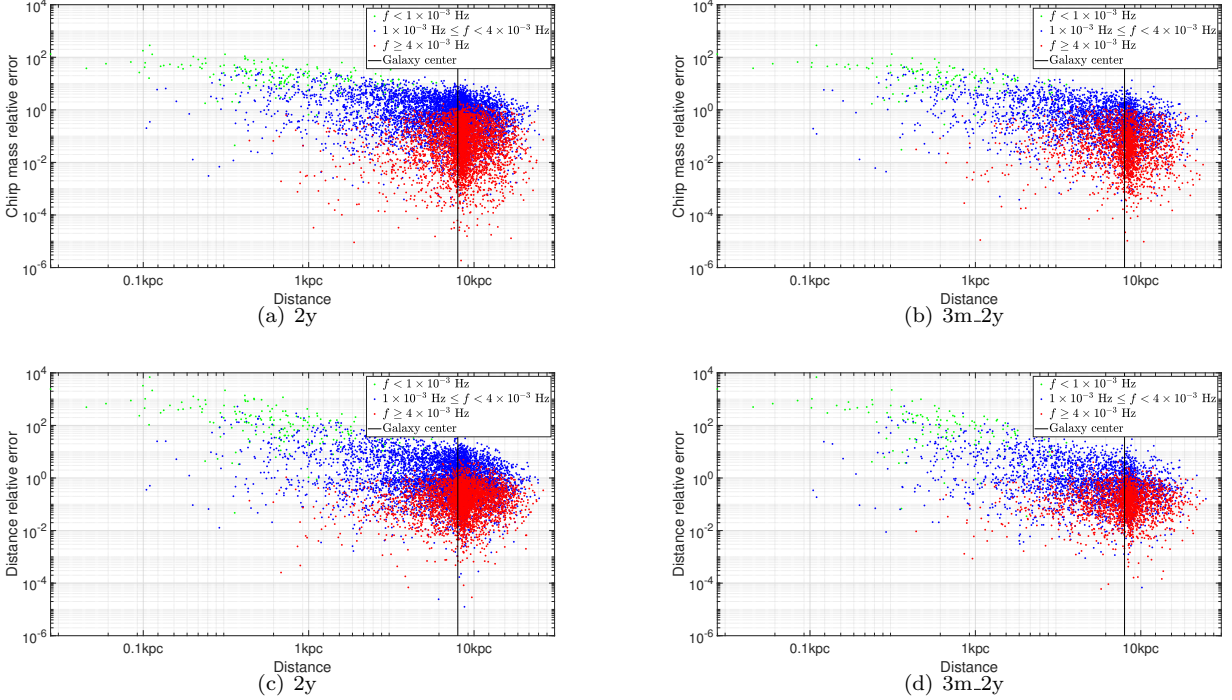


Figure 17. The relative error of chirp mass and distance of the confirmed source obtained through direct-search and accelerate-search to the two-year data. The x-axis is the distance between the source and the sun. The black line represents the location of the galactic center.

from the merger, Fig. 11) in LISA detector TDI A under different noise assumptions (Fig. 10). When only LISA instrument noise is considered, the SNR is 135.7. For original LDC1-4 data without subtracting the signals, the SNR is 99.8. In the case of direct-search and accelerate-search to the two-year data, the SNR of MBHB is 121.3 and 112.0, respectively (Tab. II).

In the context of the iterative extraction algorithm, imprecise subtraction can result in residual data contamination that could subsequently affect the accuracy of future searches. We have observed that the degree of contamination tends to rise in proportion to the number of subtraction sources and the reduction in data length (Fig. 12), and the SNR of DWD (Tab. III) is more sensitive to different noise assumptions than that of MBHB. Additionally, several questions remain unanswered, such as the potential impact of contamination on the four intrinsic parameters. Our team intends to delve deeper into this topic in future research endeavors.

We discuss LISA’s ability to explore the Milky Way structure by the detected DWD binaries (Fig. 15 and Fig. 16). The distribution of selected injection sources ($\text{SNR} \geq 3$ over two-year detection) reveals the most promising detected area of the Milky Way by LISA (Fig. 16(b)). Fig. 16(c) and Fig. 16(d) present the confirmed sources distribution from direct-search and accelerate-search to the two-year data, respectively. For confirmed sources (Fig. 17) in the high-frequency range

($f \geq 4 \times 10^{-3}$ Hz), the latitude and longitude errors are 1.3° and 0.3° , respectively. Moreover, the relative error of chirp mass and distance can reach about 20%. It implies that detecting the DWD binary through LISA could be a powerful tool for studying the Milky Way and could be complementary to electromagnetic wave detection methods.

To prepare for the future real observational stage, we also propose an SNR detection threshold for the blind search in the case of unknown injection parameter sets. As we can see from Fig. 18(b) and Fig. 18(c), the SNR threshold η should be set to 16 for the sources with $f < 4 \times 10^{-3}$ Hz and 9 for those with $f \geq 4 \times 10^{-3}$ Hz. Thus a low FAR and a high DB can be ensured simultaneously.

ACKNOWLEDGMENTS

We acknowledge valuable input from our anonymous referee. This work is supported by National Key R&D Program of China (2020YFC2201400), and by the NSFC (No. 11920101003, No. 11922303, No. 12021003 and No. 12005016). X. Fan. is supported by Hubei province Natural Science Fund for the Distinguished Young Scholars (2019CFA052). Z. Cao was supported by “the Interdisciplinary Research Funds of Beijing Normal University” and CAS Project for Young Scientists in Basic Research YSBR-006.

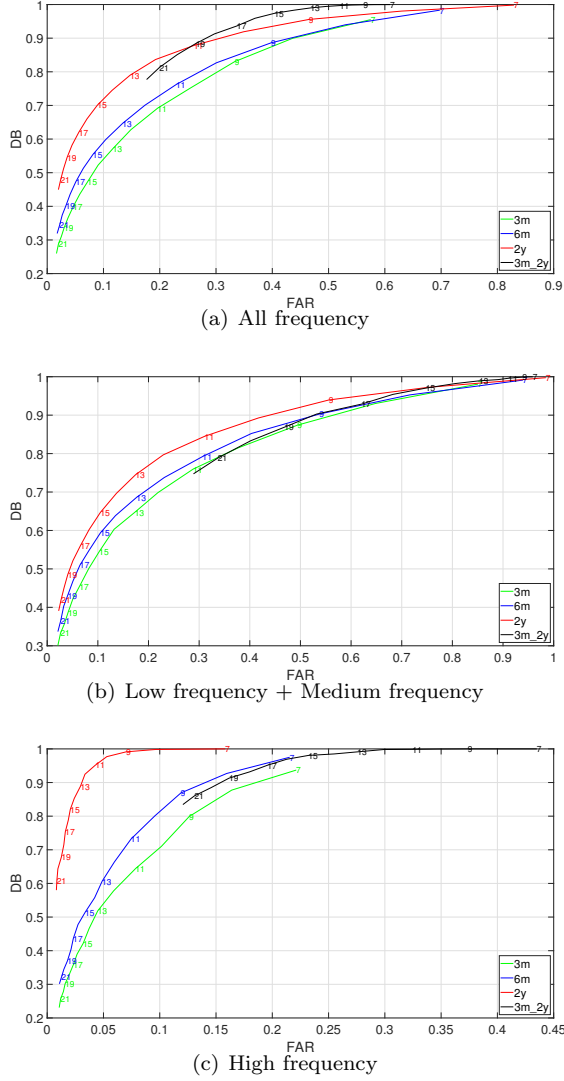


Figure 18. The top, middle, and bottom figures are the ROC diagrams for all frequencies (1×10^{-4} Hz– 1.5×10^{-2} Hz, Fig. 18(a)), low and medium frequencies (1×10^{-4} Hz– 4×10^{-3} Hz, Fig. 18(b)), high frequencies (4×10^{-3} Hz– 1.5×10^{-2} Hz, Fig. 18(c)), respectively. Each diagram contains four search situations. The color numbers in the diagram indicate the SNR threshold η of the corresponding points. The closer the point is to the upper left corner of the diagram, the closer the reported sources filtered from the corresponding SNR threshold η are to the confirmed sources.

[1] B. P. Abbott, R. Abbott, T. D. Abbott, M. R. Abernathy, F. Acernese, K. Ackley, C. Adams, T. Adams, P. Addesso, R. X. Adhikari, and V. B. Adya (LIGO Scientific Collaboration and Virgo Collaboration), Observation of gravitational waves from a binary black hole merger, *Phys. Rev. Lett.* **116**, 061102 (2016).
 [2] LISA Laser Interferometer Space Antenna.pdf, <https://arxiv.org/ftp/arxiv/papers/1702/1702.00786.pdf>

(2017).
 [3] J. Baker, J. Bellovary, P. L. Bender, et al., *The Laser Interferometer Space Antenna: Unveiling the Millihertz Gravitational Wave Sky* (2019), arXiv:1907.06482 [astro-ph, physics:gr-qc].
 [4] X. Gong, S. Xu, S. Bai, Z. Cao, et al., A scientific case study of an advanced LISA mission, *Classical and Quantum Gravity* **28**, 094012 (2011).

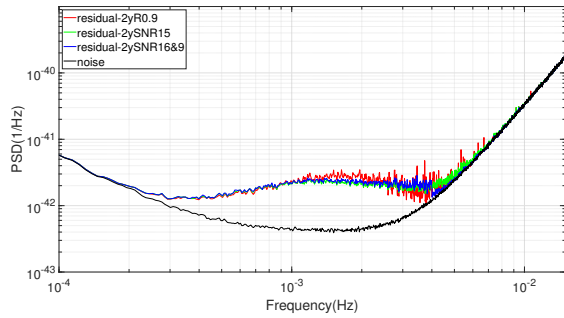


Figure 19. The red line represents residual from confirmed sources, the same as the red line in Fig. 10(c). The green line is the residual obtained from sources with $\text{SNR} \geq 15$ in all frequency domains (1×10^{-4} Hz– 1.5×10^{-2} Hz). And the blue line is the residual obtained from sources with $\text{SNR} \geq 16$ in low and medium-frequency domains (1×10^{-4} Hz– 4×10^{-3} Hz) together with $\text{SNR} \geq 9$ in high-frequency domains (4×10^{-3} Hz– 1.5×10^{-2} Hz). The black line denotes LISA instrumental noise PSD.

- [5] W.-H. Ruan, Z.-K. Guo, R.-G. Cai, and Y.-Z. Zhang, Taiji program: Gravitational-wave sources, *International Journal of Modern Physics A* **35**, 2050075 (2020).
- [6] W.-R. Hu and Y.-L. Wu, The Taiji Program in Space for gravitational wave physics and the nature of gravity, *National Science Review* **4**, 685 (2017).
- [7] The Taiji Scientific Collaboration, Y.-L. Wu, Z.-R. Luo, J.-Y. Wang, et al., China’s first step towards probing the expanding universe and the nature of gravity using a space borne gravitational wave antenna, *Communications Physics* **4**, 34 (2021).
- [8] J. Luo, L.-S. Chen, H.-Z. Duan, et al., TianQin: a space-borne gravitational wave detector, *Classical and Quantum Gravity* **33**, 035010 (2016).
- [9] J. Mei, Y.-Z. Bai, J. Bao, et al., The TianQin project: current progress on science and technology, *Progress of Theoretical and Experimental Physics* **10.1093/ptep/ptaa114** (2020), arXiv: 2008.10332.
- [10] J. Luo, Y.-Z. Bai, L. Cai, et al., The first round result from the TianQin-1 satellite, *Classical and Quantum Gravity* **37**, 185013 (2020).
- [11] T. Robson, N. J. Cornish, and C. Liu, The construction and use of LISA sensitivity curves, *Classical and Quantum Gravity* **36**, 105011 (2019).
- [12] N. Cornish and T. Robson, Galactic binary science with the new LISA design, *Journal of Physics: Conference Series* **840**, 012024 (2017).
- [13] K. A. Arnaud, S. Babak, J. G. Baker, M. J. Benacquista, N. J. Cornish, C. Cutler, S. L. Larson, B. S. Sathyaprakash, M. Vallisneri, A. Vecchio, and J.-Y. Vinet, The Mock LISA Data Challenges: An overview, *AIP Conference Proceedings* **873**, 619 (2006), arXiv: gr-qc/0609105.
- [14] K. A. Arnaud, S. Babak, J. G. Baker, M. J. Benacquista, N. J. Cornish, C. Cutler, L. S. Finn, S. L. Larson, T. Littenberg, E. K. Porter, M. Vallisneri, A. Vecchio, and J.-Y. Vinet, An overview of the second round of the Mock LISA Data Challenges, *Classical and Quantum Gravity* **24**, S551 (2007), arXiv: gr-qc/0701170.
- [15] S. Babak, J. G. Baker, M. J. Benacquista, N. J. Cornish, J. Crowder, et al., Report on the second mock LISA data challenge, *Classical and Quantum Gravity* **25**, 114037 (2008).
- [16] S. Babak, J. G. Baker, M. J. Benacquista, N. J. Cornish, S. L. Larson, et al., The Mock LISA Data Challenges: from challenge 3 to challenge 4, *Classical and Quantum Gravity* **27**, 084009 (2010).
- [17] LDC-manual-Sangria.pdf, <https://lisa-ldc.lal.in2p3.fr/> (2020).
- [18] S. D. Mohanty and R. K. Nayak, Tomographic approach to resolving the distribution of LISA Galactic binaries, *Physical Review D* **73**, 083006 (2006).
- [19] A. Stroer, J. Veitch, R.oever, et al., Inference on white dwarf binary systems using the first round Mock LISA Data Challenges data sets, *Classical and Quantum Gravity* **24**, S541 (2007), arXiv: 0704.0048.
- [20] J. Crowder and N. J. Cornish, Extracting galactic binary signals from the first round of Mock LISA Data Challenges, *Classical and Quantum Gravity* **24**, S575 (2007).
- [21] R. Prix and J. T. Whelan, F-statistic search for white-dwarf binaries in the first Mock LISA Data Challenge, *Classical and Quantum Gravity* **24**, S565 (2007), arXiv: 0707.0128.
- [22] X.-H. Zhang, S. D. Mohanty, X.-B. Zou, and Y.-X. Liu, Resolving Galactic binaries in LISA data using particle swarm optimization and cross-validation, *Physical Review D* **104**, 024023 (2021).
- [23] T. B. Littenberg, Detection pipeline for Galactic binaries in LISA data, *Physical Review D* **84**, 063009 (2011).
- [24] A. Błaut, S. Babak, and A. Królak, Mock LISA data challenge for the Galactic white dwarf binaries, *Physical Review D* **81**, 063008 (2010).
- [25] T. B. Littenberg, N. J. Cornish, K. Lackeos, and T. Robson, Global analysis of the gravitational wave signal from Galactic binaries, *Physical Review D* **101**, 123021 (2020).
- [26] S. H. Strub, L. Ferraioli, C. Schmelzbach, S. C. Stähler, and D. Giardini, Bayesian parameter-estimation of Galactic binaries in LISA data with Gaussian Process Regression, arXiv:2204.04467 [astro-ph, physics:gr-qc, physics:physics] (2022), arXiv: 2204.04467.
- [27] Y. Lu, E.-K. Li, Y.-M. Hu, J. dong Zhang, and J. Mei, An implementation of galactic white dwarf binary data analysis for mlcd-3.1, *Research in Astronomy and Astrophysics* **23**, 015022 (2023).
- [28] X.-H. Zhang, S.-D. Zhao, S. D. Mohanty, and Y.-X. Liu, *Resolving Galactic binaries using a network of space-borne gravitational wave detectors* (2022), arXiv:2206.12083 [gr-qc].
- [29] Z.-W. Han, H.-W. Ge, X.-F. Chen, and H.-L. Chen, Binary Population Synthesis, *Research in Astronomy and Astrophysics* **20**, 161 (2020).
- [30] K. A. Postnov and L. R. Yungelson, The Evolution of Compact Binary Star Systems, *Living Reviews in Relativity* **17**, 3 (2014).
- [31] T. R. Marsh, G. Nelemans, and D. Steeghs, Mass Transfer between Double White Dwarfs, *Monthly Notices of the Royal Astronomical Society* **350**, 113 (2004), arXiv:astro-ph/0312577.
- [32] L. Sberna, A. Toubiana, and M. C. Miller, Golden galactic binaries for LISA: Mass-transferring white dwarf black hole binaries, *The Astrophysical Journal* **908**, 1 (2021).
- [33] A. Stroer and A. Vecchio, The LISA verification binaries, *Classical and Quantum Gravity* **23**, S809 (2006).

- [34] W. Martens and E. Joffre, Trajectory Design for the ESA LISA Mission, [arXiv:2101.03040 \[gr-qc\]](#) (2021), arXiv:2101.03040.
- [35] J. W. Armstrong, F. B. Estabrook, and M. Tinto, Time-Delay Interferometry for Space-based Gravitational Wave Searches, *The Astrophysical Journal* **527**, 814 (1999).
- [36] M. Tinto and S. V. Dhurandhar, Time-Delay Interferometry, *Living Reviews in Relativity* **17**, 6 (2014).
- [37] M. Tinto, F. B. Estabrook, and J. W. Armstrong, Time delay interferometry with moving spacecraft arrays, *Physical Review D* **69**, 082001 (2004).
- [38] P. Jaranowski, A. Królak, and B. F. Schutz, Data analysis of gravitational-wave signals from spinning neutron stars: The signal and its detection, *Physical Review D* **58**, 063001 (1998).
- [39] A. Petiteau, G. Auger, H. Halloin, O. Jeannin, E. Plagnol, S. Pireaux, T. Regimbau, and J.-Y. Vinet, LISACode: A scientific simulator of LISA, *Physical Review D* **77**, 023002 (2008).
- [40] J. Kennedy and R. Eberhart, Particle Swarm Optimization, (1995).
- [41] Note that, since there are always DWD GW signals in the data, this detection definition is not the same as the transient signal search.
- [42] T. Robson, N. J. Cornish, and C. Liu, The construction and use of LISA sensitivity curves, *Classical and Quantum Gravity* **36**, 105011 (2019).
- [43] C. J. Moore, R. H. Cole, and C. P. L. Berry, Gravitational-wave sensitivity curves, *Classical and Quantum Gravity* **32**, 015014 (2015).
- [44] V. Korol, E. M. Rossi, P. J. Groot, G. Nelemans, S. Toonen, and A. G. A. Brown, Prospects for detection of detached double white dwarf binaries with Gaia, LSST and LISA, *Monthly Notices of the Royal Astronomical Society* **470**, 1894 (2017).
- [45] V. Korol, O. Koop, and E. M. Rossi, Detectability of Double White Dwarfs in the Local Group with LISA, *The Astrophysical Journal* **866**, L20 (2018).
- [46] A. Lamberts, S. Blunt, T. Littenberg, S. Garrison-Kimmel, T. Kupfer, and R. Sanderson, Predicting the LISA white dwarf binary population in the Milky Way with cosmological simulations, *Monthly Notices of the Royal Astronomical Society* **490**, 5888 (2019), arXiv:1907.00014.
- [47] V. Korol, E. M. Rossi, and E. Barausse, A multimessenger study of the Milky Way's stellar disc and bulge with LISA, *Gaia*, and LSST, *Monthly Notices of the Royal Astronomical Society* **483**, 5518 (2019).
- [48] V. Korol, S. Toonen, A. Klein, V. Belokurov, F. Vincenzo, R. Buscicchio, D. Gerosa, C. J. Moore, E. Roebber, E. M. Rossi, and A. Vecchio, Populations of double white dwarfs in Milky Way satellites and their detectability with LISA, *Astronomy & Astrophysics* **638**, A153 (2020).
- [49] M. Georgousi, N. Karnesis, V. Korol, M. Pieroni, and N. Stergioulas, Gravitational Waves from Double White Dwarfs as probes of the Milky Way, [arXiv:2204.07349 \[astro-ph, physics:gr-qc, physics:physics\]](#) (2022), arXiv:2204.07349.